PLANETARY SCIENCE

A partially equilibrated initial mantle and core indicated by stress-induced percolative core formation through a bridgmanite matrix

Lin Wang[1,2]* and Yingwei Fei[1]*

The Earth's core formation mechanism determines the siderophile and light elements abundance in the Earth's mantle and core. Previous studies suggest that the sink of massive liquid metal through a solid silicate mantle resulted in an unequilibrated core and the lower mantle. Here, we show that percolation can be an effective core formation mechanism in a convective mantle and modify the compositions of the lower mantle and the core through partial equilibration between them. This grain-scale metal flow has a high velocity to meet the time constraint of core formation. The Earth's core could have been enriched with light elements, and the abundance of the moderately siderophile elements in the mantle could have been elevated to the current value during this process. The trapped core-forming melt in the mantle during the stress-induced percolation can also explain the highly siderophile element abundance in the Earth's mantle.

INTRODUCTION

The segregation of the core and mantle is the most important event in the evolutionary history of Earth, which shapes the layered structure, dynamic convection, and composition differentiation in geological time. The migration of iron-rich core-forming melt to the center of the planet causes the depletion of siderophile elements in the mantle (*1*–*5*) and the enrichment of light elements in the core (*6*–*8*). Knowledge of core formation mechanisms is therefore essential to explain the siderophile element abundances in the mantle and light element budget in the core. The interaction between the core-forming melts and mantle is also necessary to understand the large-scale geophysical evolution of the planet (*9*).

The segregation of core-forming melts from silicates in Earth involves settling iron alloy melts through a magma ocean and solid silicate mantle (*2*, *10*). The latter occurs when the descending alloy reaches the depth where the large portion of the mantle has already solidified. Geochemical evidence suggests that the terrestrial magma ocean was not sufficiently deep to cover the entire mantle (*5*, *11*). The segregation of core-forming melt in a solid silicate matrix was therefore inevitable on a big planet such as Earth.

Metallic melt can percolate through the grain boundary. As a grain-scale melt flow, percolation could result in an equilibrium between the core and the lower mantle. On the other hand, core-forming melt can also descend through the underlying solid silicate massively as diapirs or by dyking when the accumulated melt at the bottom of the magma ocean reaches a critical thickness (*12*, *13*). Because of the large volume of the descending metal, diapirs and dyking do not alter the composition of core melt and surrounding mantle (*2*, *14*).

Percolation, however, has been ruled out by hydrostatic annealing experiments as a core formation mechanism. Under hydrostatic conditions, the efficiency of percolation is determined by the interfacial energy of the liquid and solid, which is reflected by the dihedral angle (θ) between two neighboring solid grains in contact with the melt at a triple junction. When θ is less than 60°, the melt can form an interconnected network irrespective of melt fraction through which complete melt drainage via percolation is possible (*15*). Previous hydrostatic annealing experiments have suggested that $\theta > 60°$ for an iron alloy–silicate matrix system at pressures less than 60 GPa (*16*–*22*), indicating that percolation cannot be an efficient core formation mechanism under hydrostatic conditions.

The situation could change under the dynamic conditions. The isostatic adjustments after a large impact (*23*) and heat-induced mantle convection would make the solid silicate mantle continually deforming. The melt texture developed under hydrostatic conditions could have been continually perturbed by the convective straining of the matrix. This perturbation is not negligible especially for early Earth where mantle convection is vigorous (*10*). The melt texture developed under these deforming conditions is controlled by the balance between the external stress and interfacial tension of the liquid pocket (*24*, *25*). If the stress is higher than the surface tension, then the melt could also be interconnected, although the dihedral angle is larger than 60°. Therefore, it is necessary to study percolation behavior under deformation with more definitive criteria for melt interconnectivity to understand the differentiation process.

In this study, we provide the first look on the effect of stress on the percolative behavior of core-forming melt in a bridgmanite matrix. Although it has been shown that metallic melt can form an interconnected network by deformation under low pressures (*24*–*29*), the effect of deformation on the percolation of iron alloy at high pressure remains virtually unknown owing to a lack of experimental data. At high pressure, bridgmanite is the dominant mantle phase and therefore plays a critical role in metal-silicate separation after core-forming melts settle to the bottom of the magma ocean. Thus, we focus on the stress effect on the percolation of core-forming melt in a bridgmanite matrix.

Fe-S melt is used in this study to represent the core-forming melt. The percolation behavior of this iron alloy has been

[1]Earth and Planetary Laboratory, Carnegie Institute for Science, Washington, DC, USA. [2]Bayerisches Geoinstitut, University Bayreuth, Bayreuth, Germany.
*Corresponding author. Email: lin.wang@uni-bayreuth.de (L.W.); yfei@carnegiescience.edu (Y.F.)

extensively investigated under hydrostatic conditions (*16*, *17*, *19*) and, therefore, allowing a direct comparison between our results and previous ones. In addition, although S can decrease the interfacial energy of iron melt and favor the stress-induced percolation, the extent is much less than other elements, such as O (*19*, *21*). Here, we experimentally demonstrate that Fe-S melts can form an interconnected network in the bridgmanite matrix under deformation and discuss its implication for the composition of the Earth's core and mantle.

RESULTS

A deformation experiment was conducted at 24 GPa and 2100 K using the multianvil apparatus at Bayerisches Geoinstitut (BGI). The sintered aggregation of 5 volume % of Fe-S alloy [6 weight % (wt %) of S] and 95 volume % of bridgmanite $(Mg_{0.9}Fe_{0.1})SiO_3$ together with a Re strain marker was inserted into a Pt holder and sheared by two 45°-cut hard alumina pistons (fig. S1A). An experiment without deformation (annealing run) using the same cell assembly as the deformation run was conducted to directly compare the deformed and undeformed samples under the same conditions. Because hard alumina pistons could introduce high stress on the sample during cold compression, we also used crushable alumina pistons in an additional annealing experiment (fig. S1B). Experimental conditions are shown in table S1.

Run products after synthesis, annealing, and deformation

Bridgmanite was successfully synthesized judging from the run product textures and composition analysis (fig. S2). A secondary electron image (fig. S2) of the sintered aggregation reveals that the Fe-S alloy was evenly distributed in the bridgmanite matrix. Some minor Fe-rich (Mg,Fe)O also formed during the synthesis possibly because of Fe oxidation during the experiments (*30*).

Backscattered electron images and Pt mappings of undeformed and deformed samples are shown in Figs. 1 and 2, respectively. The strain marker did not rotate in the annealing run (Fig. 1A), indicating no deformation. On the other hand, there is a rotation of 41° ± 3° in the deformation run (Fig. 2A), indicating 0.87 ± 0.09 strain. In addition, the boundaries between the Pt holder and sample did not rotate in the annealing run (Fig. 1A) while rotated to a similar extent as the strain marker in the deformation run (Fig. 2A). Therefore, the boundaries between Pt holder and sample can also indicate whether the sample was deformed. For the annealing experiments, we also compared the effect with hard and crushable alumina pistons (Fig. 1, A and B). Judging from the boundary between Pt holder and sample, there is no deformation in the annealing run with the crushable alumina piston (Fig. 1B).

The Fe-S melt in the undeformed sample exhibits isolated pockets (Fig. 1, C and D) with an average apparent dihedral angle of 77° ± 35° (fig. S3). The quenched metallic melts contain a typical dendric Fe-S melt quench texture (Fig. 1D), indicating that the iron alloy was fully molten at the experimental temperature. The average composition of the melts is close to that of the starting metal alloy. All melt pockets have a diameter of less than 15 μm. The distribution and topology of the metallic melt are similar to those reported in previous studies without deformation (*19*).

In contrast, the melt pockets in the deformed sample are elongated (Fig. 2, B and C). Some of these pockets are aligned and form planes with an angle of ~15° from the shear plane (Fig. 2C). Similar textures were reported in iron alloy in a deformed olivine matrix (*24*–*27*). These melt pockets distribute in the grain scale and did not form bands with a high melt fraction (*24*, *27*, *31*). The dihedral angle of Fe-S melt is 79° ± 19° (fig. S4).

The texture equilibrium should have been reached in our experiments. For the annealing experiments, we annealed the sample for 120 min, which is sufficient for texture equilibrium compared with previous studies. For example, multianvil experiments (*32*) reported that the steady-state texture is reached within 50 min at 15 GPa and 2000 K. A recent study also reported that 30 min is enough for texture equilibrium at 23 GPa and 2100 K in their multianvil experiments (*33*). In addition, the distribution of the dihedral angles can be fitted by Gaussian curves (fig. S3), indicating sufficient approach to texture equilibrium. Equilibrium is further supported by the nearly 120° of dihedral angles at triple junctions of bridgmanite grains (Fig. 1D). The texture equilibrium in the deformed sample can also be inferred. Our deformation time is 120 min, which is two times longer than that in the texture study of deformation in bridgmanite (*34*). In addition, deformation experiments suggested that the steady-state deformation in the metal melt–silicate system can be reached with 30 min (*25*). They also suggested that the general deformation style is determined nearly at the beginning of deformation and changes little with time.

Melt composition in the deformed and undeformed samples

Only melt near Pt holder shows some Pt contamination in the undeformed sample (Fig. 1, E and F), whereas Pt and Re are found throughout the melt in the deformed sample (Fig. 2, C and D). The Pt mapping clearly shows the difference in the Pt distribution in the undeformed (Fig. 1, E and F) and deformed samples (Fig. 2D). The Re content of melts in the deformed sample is 2.0 ± 0.2 atomic %, S content is 11 ± 2 atomic %, and the Pt content ranges from 5 to 10 atomic % (table S2). We also found a few isolated Fe-S melt pockets among the Fe-Pt-Re-S melt in the deformed sample (Fig. 2C).

Stress-induced melt network in a deformed bridgmanite matrix

The composition of melt provides definitive evidence for melt interconnection by deformation. The distinct melt compositions in the deformed and undeformed sample demonstrate that either (i) an interconnected Fe-S melt network formed by deformation through which Pt and Re migrated from the Pt holder and Re strain marker into the melt or (ii) Fe-Pt-Re-S melts formed at the sample-metal interface and then extended into the sample and connected Fe-S melt pockets during deformation. The second scenario indicates that stress can make Pt-Fe-Re-S melts forming melt channels. Re has a similar interfacial energy with Fe, but Pt has a much higher interfacial energy than Fe (*35*). The resulting Fe-Pt-Re-S melts should have higher interfacial energy than Fe-S melts, which should prohibit the formation of a melt network compared with Fe-S melts. Therefore, our results demonstrate that stress can make Fe-S melt interconnected in either case.

The similar composition in the nearby melt pockets (Fig. 2B) also proved that these melts are interconnected. These aligned melt pockets provide an additional evidence of melt interconnectivity.

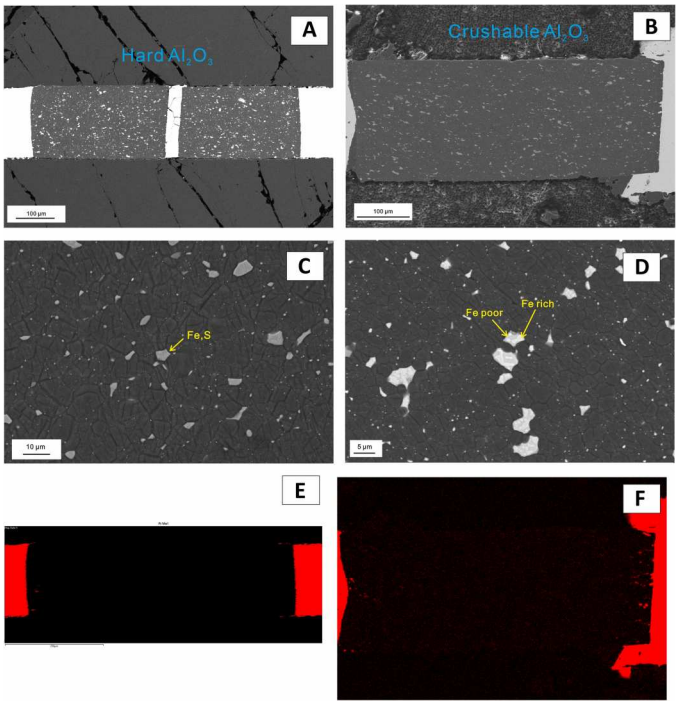

Fig. 1. Backscattered electron images and Pt mappings of undeformed samples. (**A**) Undeformed sample using hard alumina pistons. (**B**) Undeformed sample using crushable alumina pistons. (**C**) Isolated Fe-S melt pockets. (**D**) Dendric texture showing melting of the Fe-S. (**E**) Pt mapping of (A). (**F**) Pt mapping of (B).

The dihedral angle of 79° in the deformed sample does not contradict with the interconnection of melt in the deformed sample. The dihedral angle is only a useful indication for interconnection under hydrostatic conditions. A higher than 60° dihedral angle of interconnected iron melt in silicate is also reported by a previous study (*27*). Actually, the dihedral angle in the deformed sample shows binary distribution to some extent and covers a wider range than the one in the undeformed sample. This is a sign of deformation of melt.

The absence of Pt in the melts in the undeformed sample indicates that Fe-S was not interconnected in the bridgmanite matrix under static conditions, although the system contained 5 volume % of melt. The critical melt amount for interconnection in a system with a dihedral angle of 77° is 3 volume % (*15*). A higher critical melt amount for interconnection than the theoretical value was also reported in previous experimental studies. For example, in the FeS-olivine system with a dihedral angle of 75° (*22*), the measured percolation threshold was 5 volume % (*36*). One possible explanation for this discrepancy is that the theoretical value of critical melt amount for an interconnected network was deduced under the assumption of a perfect distribution of melt in the solid matrix (*22*). Further experimental studies on the percolation threshold may reconcile this discrepancy.

DISCUSSION

Scaling to the Earth conditions

A scaling method was used to account for the different strain rates in the experiment and real Earth (*25*). High–surface energy melt pockets tend to form a network under dynamic conditions if the external stress is higher than the melt surface tension (stress controlled); otherwise, the melt pockets tend to remain as individual droplets (surface tension controlled). Because a melt pocket with a smaller size (r) has a larger surface tension, the melt pockets tend to be interconnected at high stress (or high strain rate $\dot{\varepsilon}$) and large r while remaining isolated at low $\dot{\varepsilon}$ and small r. The size of the largest undeformed melt pocket (r_{max}) defines the upper limit of the surface tension–controlled regime, and the size of the smallest deformed pocket (r_{min}) defines the lower limit of the stress-controlled regime. It was suggested that r_{max} and r_{min} forms lines with a negative slope of $-1/n$ in the $\log(r)$-$\log(\dot{\varepsilon})$ plot, where n is controlled by the deformation mechanism of the solid phase (*25*).

Using this scaling method, we extrapolate our results to the real Earth situation. Our deformation experiment has r_{min} of ~1 μm and r_{max} of ~5 μm. The $\dot{\varepsilon}$ in our experiment is ~10^{-4}. Assuming that the bridgmanite deformation is controlled by dislocation creep (*37*) and has the same n = 3.5 as olivine dislocation creep (*38*), the regime where the melt distribution is controlled by stress can be identified in the $\log(r)$-$\log(\dot{\varepsilon})$ plot (fig. S5). Because the melt pocket sizes in early Earth are unknown, we use the diameter of metallic melt pockets in meteorites instead (*39*, *40*). The strain rate in the current Earth's mantle is 10^{-12} to 10^{-14} (*25*). The melt texture in real Earth could therefore fall in the stress-dominated regime (fig. S5). The mantle in early Earth could have also had a higher strain rate (*10*), which would further move the melt texture under natural conditions into the stress-dominated regime (fig. S5).

A recent study (*29*) even suggested that deformation-aided melt segregation could be independent of the strain rate at high pressure, implying that no scaling is required to apply the experimental results to the natural environment. Stress-induced percolation could therefore occur during metal-silicate segregation in early Earth.

Although the S concentration in the melt in our sample is higher than the value expected in the Earth's core (*6*–*8*), the interconnection of core-forming melt with an Earth's core composition should also be established by deformation. Decreasing the S content can increase the dihedral angle and prevent formation of interconnection. However, there are some other surface active elements such as O and Si, which could also play a role in enhancing interconnectivity. Assuming a core with 0.8 wt % of O (*8*), adding 0.8 wt % of O to the melt can decrease the dihedral angle by 20°, equivalent to adding 12 wt % of S (*21*). Therefore, adding an element such as O would further facilitate the interconnection under deformation. On the other hand, it was (*26*) demonstrated that both Au melt with a dihedral angle of 150° and Fe-Ni-S melt with a dihedral angle of 75° can be interconnected in olivine under deformation, indicating that the melt composition may play a secondary role in the stress-induced percolation.

Pressure should also favor the stress-induced percolation. The dihedra angle of iron alloy decreases with pressure (*17*, *19*, *20*). This indicates that the interfacial tension of melt pockets decreases with pressure. Therefore, it is easier to form an interconnected network of melt by deformation at higher pressure. When pressure

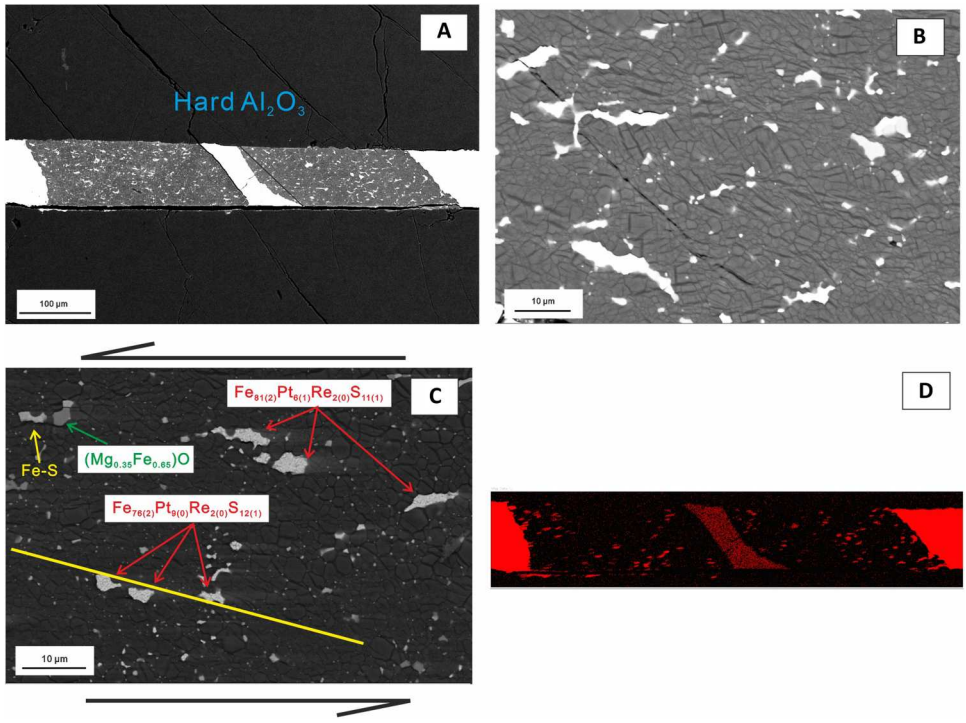

Fig. 2. Backscattered electron images and Pt mapping of the deformed sample. (**A**) Deformed sample at 24 GPa and 2100 K. The Re strain marker rotated ~41°, indicating a strain of ~0.8. (**B**) Elongated melt pockets. (**C**) Aligned Fe-Pt-Re-S melt pockets (red arrows) form planes subparallel to the shear direction (black arrows). The intersection of one such plane with the page is shown by the yellow line. The compositions of the melt pockets are shown. The numbers in the parentheses indicate the errors. These melt pockets show two different compositions and should be stemmed from different melt channels. Some Fe-S (yellow arrow) and (Mg,Fe)O (green arrow) are also found in the sample. (**D**) Pt mapping of sample. The shear direction is shown in (C).

is high enough that dihedral angle goes below 60°, percolation can happen without stress. However, deformation can increase the permeability and make the percolation more efficient (*24*).

Time scale of stress-induced percolation as a core formation mechanism

The time required by core-forming melts to percolate through the mantle can be calculated from the segregation velocity (V_m), which is expressed as (*41*, *42*)

$$V_m = \frac{k\Delta\rho g}{\varphi\mu} \quad (1)$$

where Δρ is the density difference between the solid and liquid (3500 kg/m^3), μ is the melt viscosity, taken as 0.04 Pa·s (*43*), φ is the melt fraction, g is the acceleration due to gravity, and k is the permeability, which can be expressed as (*27*)

$$k = \frac{d^2\varphi^n}{C} \quad (2)$$

where d is grain size and C is a constant that depends on the melt network geometry. Many studies have estimated the V_m of core-forming melts in silicate (*15*, *27*, *41*, *42*, *44*–*48*), and n ranging from 1 to 3.8 was proposed (*42*, *47*). Accordingly, the estimated V_m varies by orders of magnitude. Here, we estimate the V_m using a theoretical model where melt moves in a network of interconnected tubules (*27*), where $C = 72\pi$ and $n = 2$, and an experimental result for melt migration (*47*), where $C = 250$ and $n = 3.6$. The study (*47*) is the only experimental study that has systematically investigated the parameters in Eq. 2 in the metal-silicate system.

The calculated V_m (Fig. 3) indicates that the percolation of core-forming melts is sufficiently fast to meet the time-scale constraint of the core formation from geochemical evidence. Recent grain growth experiments (*49*) indicated that a 1-Ma-old lower mantle would have bridgmanite with grain size greater than 70 μm assuming a 200-K higher mantle temperature than the present one (*50*). With a melt fraction of 0.1, the calculated V_m values using the theoretical (Fig. 3A) and experimental (Fig. 3C) model are 58 and 1.3 meters/year, respectively. This requires less than 2 Ma to drain the melts through a 2000-km-thick Earth's lower mantle, which is within the 30-Ma duration for core formation based on mantle Hf-W isotopic ratios (*51*). Stress-induced percolation is therefore an effective mechanism for the Earth's core formation.

Chemical consequence of percolation core formation

The grain scale percolation of core-forming melt leads to a substantial composition exchange between the melt and the surrounding mantle via diffusion. The diffusion distance, $d_{diffusion}$, in the surrounding mantle during the melt residence time can be expressed by (*52*)

$$d_{diffusion} = \sqrt{Dt} = \sqrt{D\frac{S}{V_m}} \quad (3)$$

where D is the diffusion coefficient and t is the melt residence time in the mantle, which is determined by the solid mantle thickness S

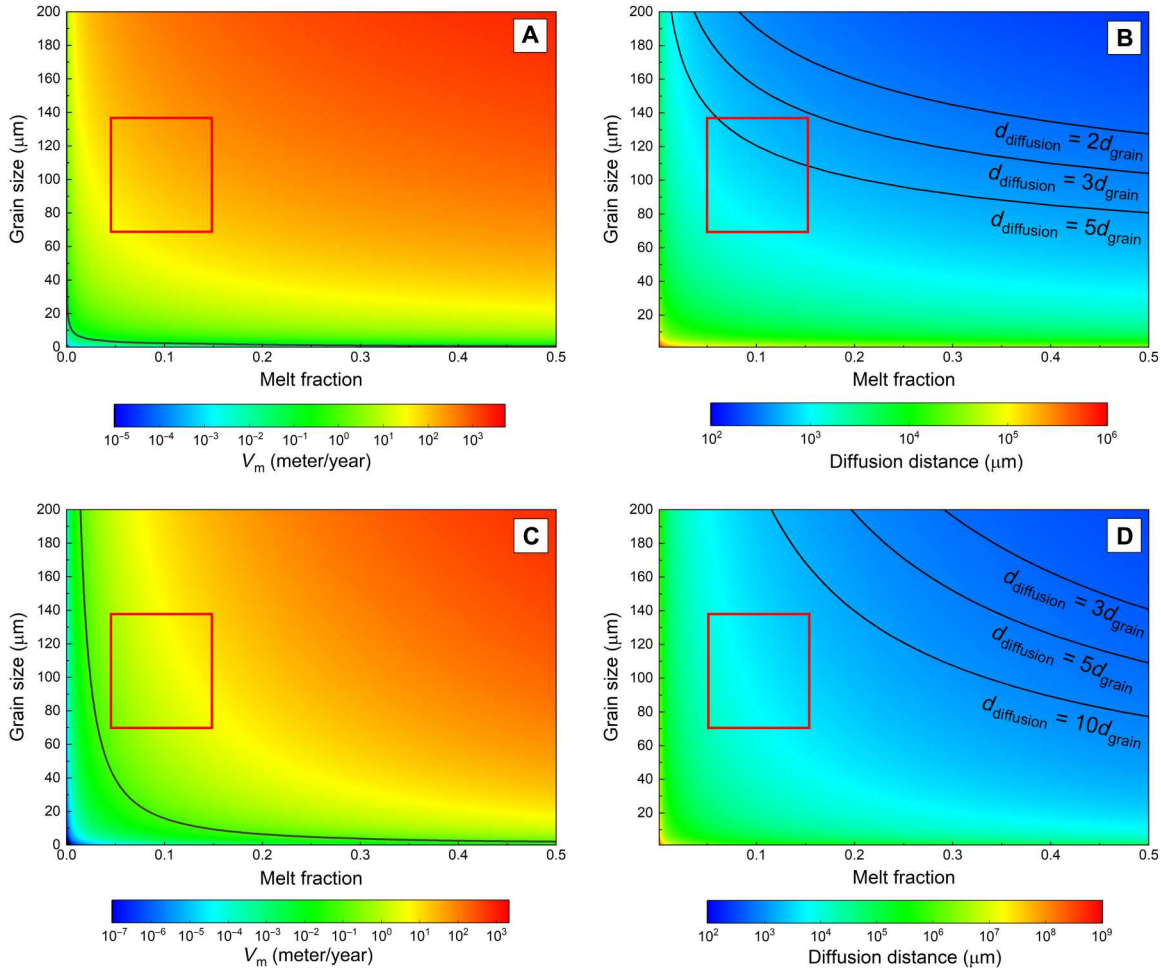

Fig. 3. Segregation velocity (V_m) as a function of melt fraction and grain size and corresponding diffusion distance. (**A** and **C**) V_m in the theoretical model and experimentally based model. The conditions above the black curve fulfill the 30-Ma time requirement of the Earth's core formation. (**B** and **D**) Diffusion distance during percolation in the models (A) and (C). The black lines indicate that diffusion distance equals to 2, 3, and 5 times of grain size in (B) and 3, 5, and 10 times of grain size in (D). The red rectangles in the figures mark the possible conditions during which the core formed. It is clear that the stress-induced percolation meets the time constraint of the Earth's core formation. The diffusion distance in the percolation is at least three times larger than the grain size.

and V_m. Taking D as the Fe-Mg interdiffusion coefficient of 10^{-18} m^2/s (*53*), a solid lower mantle of 2000 km, the diffusion distance is more than 340 μm (Fig. 3), which is larger than the bridgmanite grain size. The distance between melt channels is several grain sizes judging from our experiments and previous studies (*24*). This indicates that a substantial solid mantle could have been equilibrated with the core-forming melt. We also used different parameters in Eqs. 1 to 3 proposed by different studies. The simulation results are shown in the Supplementary Materials, and the basic conclusion remains the same.

The core-forming melt could have been enriched with light elements during percolation. At high pressure, extensive dissolution of light elements such as O and Si from lower mantle minerals into liquid iron occurred (*54*). Equilibrium between liquid iron and bridgmanite at 95 GPa and 3100 K could already account for the 7 % of density deficit of the core (*54*). Therefore, the core could have been enriched with enough light elements to explain its density deficit after core formation completed.

On the other hand, the interaction of the permeable liquid metal and the silicate mineral could also elevate the siderophile elements abundance in the lower mantle. Because of the equilibrium between core-forming melts and surrounding mantle, the siderophile element abundance in the mantle should be not only affected by the magma ocean scenario but also determined by the following segregation of liquid metal and solid silicates. A previous study has shown that the equilibrium between bridgmanite and iron-rich metal alloy at 80 GPa can explain the Ni and Co abundance in the mantle (*55*). This indicates that the percolation model is not at odds with the moderate siderophile element abundance in the Earth's mantle.

The highly siderophile element (HSE) abundance in the Earth's mantle could also have been affected by the percolation. The stress-induced percolation always leaves some amounts of melts in the mantles (*24*). These stranded melts could increase the mantle HSE abundance. The extent of the HSE enhancement in the mantle depends on the magma ocean depth, which influences the HSE contents in the liquid metal during metal-silicate equilibrium

(*56*), and the amount of the stranded melts. Our calculations indicate that with a magma ocean depth between 40 and 60 GPa, 0.1 to 1 wt % of stranded melts can reproduce the mantle HSE abundance very well (Fig. 4). Detailed calculations are provided in the Supplementary Materials. The calculated characteristic high Ru/Ir ratio is due to the larger partition coefficient of Ir compared with Ru. With the bridgmanite grain size of hundreds of micrometers, the stress of early Earth of 10^6 Pa (*24*) and the dihedral angle of 77°, about 0.1 to 2 wt % of core-forming melt could have been trapped in the mantle (*24*). Therefore, the stress-induced percolation provides an alternative explanation of HSE abundance in the mantle that does not require a late veneer hypothesis.

Last, there are some limitations about the current study. Although 0.8 strain of high-pressure phase mixture is the largest strain ever achieved in the simple shear geometry, it is still low compared with the estimated strain of early Earth. Experiments with higher strain are desired to test whether melt texture changes with strain. In addition, the percolation threshold under different strains was not determined in this study. Further studies could better constrain these parameters.

MATERIALS AND METHODS

Synthesis of starting material

Well-sintered aggregates of 5 volume % of Fe-S alloy (6 wt % of S) and 95 volume % of bridgmanite $(Mg_{0.9}Fe_{0.1})SiO_3$ were prepared using the following procedure. A glass with the desired bridgmanite composition was prepared by fusing a mixture of MgO, SiO_2, and Fe_2O_3 with the prescribed ratio at 1923 K and followed by rapid quenching in cold water, using a high-temperature furnace at the BGI, University of Bayreuth, Germany. The glass was subsequently reduced in a gas mixture furnace (CO and CO_2 gas) at 1523 K with an oxygen fugacity of one log unit above the iron-wüstite buffer for 48 hours. The synthesized enstatite powder was then mixed with Fe and FeS powder with a prescribed ratio. The mixture was compressed to 24 GPa in a multianvil apparatus using an 8-3 assembly at the Earth and Planets Laboratory (EPL) of the Carnegie Institution. After heating to 1873 K, the temperature was maintained for 2 hours to allow for the transformation to bridgmanite. The temperature was recorded using a W95%Re5%-W74%Re26% thermocouple.

Deformation and annealing experiments

Deformation experiments were conducted using the multianvil apparatus at BGI. Figure S1A shows a schematic diagram of the adopted cell assembly. The sintered starting material was shaped into a cylinder with a ~650-μm diameter and a 200-μm thickness and inserted into a Pt tube. Pt was used as an indicator for interconnectivity. If the Fe-S alloy interconnects, then Pt is expected to alloy with Fe and migrate throughout the melt. If the Fe-S remains isolated, then Pt is expected to only alloy with Fe at the sample-Pt tube interface. The sample and Pt tube were sandwiched by two 45°-cut hard alumina pistons and inserted into an MgO sleeve made from a sintered MgO rod. A 50-μm-thick Re foil was placed at the ends of each 45°-cut alumina piston to reduce the friction against sideslip during deformation (*34*). The temperature was estimated on the basis of the established power-temperature relation for the same cell assembly configuration.

The specimens were first compressed to 24 GPa (620 tons) at room temperature and then heated to 2100 K for 40 min to relax the deviatoric stress in the specimens. The press load was then increased to 760 metric tons over 2 hours to deform the sample (deformation run). Note that although the oil pressure increase, the actual pressure in the cell assembly remains nearly the same because of the flatting of the pressure generation curve (*57*). The different compressibilities of the alumina and MgO capsule result in a deviatoric stress on the sample that leads to sample shearing. The total strain (ε) is estimated from the rotation of the Re strain marker (Figs. 1A and 2A) and shape change of the sample (Fig. 1B).

We also performed an experiment without deformation (annealing run) using the same cell assembly as in the deformation run to directly compare the deformed and undeformed samples under the same conditions. For the annealing run, the specimen was directly compressed to 760 metric tons and then annealed at 2100 K for 2 hours with no additional increase in oil pressure after reaching the target temperature. Because hard alumina pistons could introduce some stress during cold compression, we also conducted an annealing experiment at EPL using crushable alumina (fig. S1B).

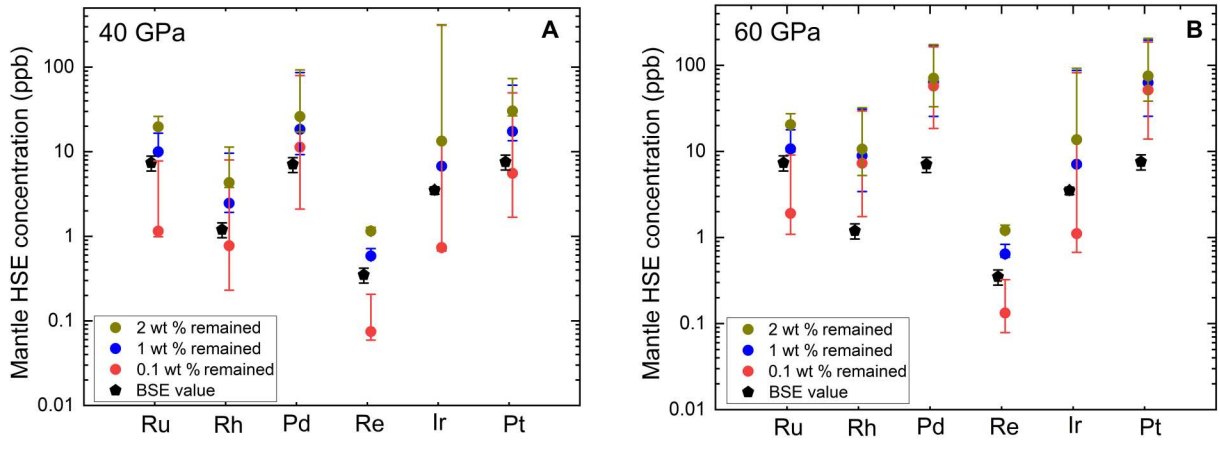

Fig. 4. Mantle HSE abundance with 0.1, 1, and 2 wt % of core-forming melt stranded in the mantle after the magma ocean. The calculation assumes liquid metal equilibrated with liquid silicate at 40 GPa (**A**) and 60 GPa (**B**) in the magma ocean. The partition coefficients of HSE were taken from (*56*). The details of the calculation are shown in the Supplementary Materials. The errors were propagated from the errors in the partitioning coefficients (*56*). ppb, parts per billion. BSE, bulk silicate Earth.

The results of an additional deformation experiment using the same cell assembly are also shown in the Supplementary Materials. In all the experiments, the temperature was quenched by shutting off the power.

Data analysis

The recovered samples were mounted in epoxy resin and sequentially polished with SiC sandpapers and diamond paste. The melt textures of the samples were observed using a field-emission scanning electron microscope at EPL and BGI. The dihedral angles of the Fe-S melts in the bridgmanite samples were measured in two-dimensional cross sections. Measurements were conducted on 121 and 130 melt pockets at triple junctions for the undeformed and deformed samples, respectively. Pt mapping of the samples and compositional analysis of the melt pockets and bridgmanite were performed using energy dispersive spectroscopy.

Supplementary Materials

This PDF file includes:

Supplementary Text
Figs. S1 to S10
Tables S1 and S2
References

REFERENCES AND NOTES

1. J. Li, C. B. Agee, Geochemistry of mantle–core differentiation at high pressure. *Nature* **381**, 686–689 (1996).
2. D. C. Rubie, F. Nimmo, H. J. Melosh, Formation of the Earth's core, in *Treatise on Geophysics*, D. Stevenson, Ed., (Elsevier, 2007), Evolution of the Earth, vol. 9, pp. 51–90.
3. J. Wade, B. Wood, Core formation and the oxidation state of the Earth. *Earth Planet. Sci. Lett.* **236**, 78–95 (2005).
4. J. F. Rudge, T. Kleine, B. Bourdon, Broad bounds on Earth's accretion and core formation constrained by geochemical models. *Nat. Geosci.* **3**, 439–443 (2010).
5. J. Siebert, J. Badro, D. Antonangeli, F. J. Ryerson, Metal–silicate partitioning of Ni and Co in a deep magma ocean. *Earth Planet. Sci. Lett.* **321**, 189–197 (2012).
6. J. Li, Y. Fei, Experimental constraints on core composition, in *Treatise on Geochemistry* (Elsevier, 2003), vol. 2, pp. 568.
7. B. J. Wood, M. J. Walter, J. Wade, Accretion of the Earth and segregation of its core. *Nature* **441**, 825–833 (2006).
8. K. Hirose, B. Wood, L. Vočadlo, Light elements in the Earth's core. *Nat. Rev. Earth Environ.* **2**, 645–658 (2021).
9. Z. Zhang, S. M. Dorfman, J. Labidi, S. Zhang, M. Li, M. Manga, L. Stixrude, W. F. McDonough, Q. Williams, Primordial metallic melt in the deep mantle. *Geophys. Res. Lett.* **43**, 3693–3699 (2016).
10. D. Stevenson, in *Origin of the Earth* (Oxford Univ. Press, 1990), pp. 231–249.
11. M. Shannon, C. Agee, High pressure constraints on percolative core formation. *Geophys. Res. Lett.* **23**, 2717–2720 (1996).
12. A. M. Rubin, Propagation of magma-filled cracks. *Annu. Rev. Earth Planet. Sci.* **23**, 287–336 (1995).
13. R. Honda, H. Mizutani, T. Yamamoto, Numerical simulation of Earth's core formation. *J. Geophys. Res. Solid Earth* **98**, 2075–2089 (1993).
14. V. R. Murthy, S.-i. Karato, Core formation and chemical equilibrium in the Earth—II: Chemical consequences for the mantle and core. *Phys. Earth Planet. In.* **100**, 81–95 (1997).
15. N. von Bargen, H. S. Waff, Permeabilities, interfacial areas and curvatures of partially molten systems: Results of numerical computations of equilibrium microstructures. *J. Geophys. Res. Solid Earth* **91**, 9261–9276 (1986).
16. M. Shannon, C. Agee, Percolation of core melts at lower mantle conditions. *Science* **280**, 1059–1061 (1998).
17. C. Y. Shi, L. Zhang, W. Yang, Y. Liu, J. Wang, Y. Meng, J. C. Andrews, W. L. Mao, Formation of an interconnected network of iron melt at Earth's lower mantle conditions. *Nat. Geosci.* **6**, 971–975 (2013).
18. W. G. Minarik, F. J. Ryerson, E. B. Watson, Textural entrapment of core-forming melts. *Science* **272**, 530–533 (1996).
19. H. Terasaki, D. J. Frost, D. C. Rubie, F. Langenhorst, Interconnectivity of Fe–O–S liquid in polycrystalline silicate perovskite at lower mantle conditions. *Phys. Earth Planet. In.* **161**, 170–176 (2007).
20. N. Takafuji, K. Hirose, S. Ono, F. Xu, M. Mitome, Y. Bando, Segregation of core melts by permeable flow in the lower mantle. *Earth Planet. Sci. Lett.* **224**, 249–257 (2004).
21. H. Terasaki, D. J. Frost, D. C. Rubie, F. Langenhorst, The effect of oxygen and sulphur on the dihedral angle between Fe–O–S melt and silicate minerals at high pressure: Implications for Martian core formation. *Earth Planet. Sci. Lett.* **232**, 379–392 (2005).
22. N. Walte, J. Becker, P. Bons, D. Rubie, D. Frost, Liquid-distribution and attainment of textural equilibrium in a partially-molten crystalline system with a high-dihedral-angle liquid phase. *Earth Planet. Sci. Lett.* **262**, 517–532 (2007).
23. W. B. Tonks, H. J. Melosh, Core formation by giant impacts. *Icarus* **100**, 326–346 (1992).
24. N. Groebner, D. L. Kohlstedt, Deformation-induced metal melt networks in silicates: Implications for core–mantle interactions in planetary bodies. *Earth Planet. Sci. Lett.* **245**, 571–580 (2006).
25. N. Walte, D. Rubie, P. Bons, D. Frost, Deformation of a crystalline aggregate with a small percentage of high-dihedral-angle liquid: Implications for core–mantle differentiation during planetary formation. *Earth Planet. Sci. Lett.* **305**, 124–134 (2011).
26. D. Bruhn, N. Groebner, D. L. Kohlstedt, An interconnected network of core-forming melts produced by shear deformation. *Nature* **403**, 883–886 (2000).
27. J. W. Hustoft, D. L. Kohlstedt, Metal-silicate segregation in deforming dunitic rocks. *Geochem. Geophys. Geosyst.* **7**, (2006).
28. T. Rushmer, W. Minarik, G. Taylor, Physical processes of core formation, in *Origin of the Earth and Moon* (University of Arizona Press, 2000), p. 227.
29. M. T. Berg, G. D. Bromiley, I. B. Butler, M. Frost, R. Bradley, J. Carr, Y. Le Godec, L. G. Montési, W. Zhu, K. Miller, J.-P. Perrillat, E. Mariani, D. Tatham, S. A. T. Redfern, Deformation-aided segregation of Fe-S liquid from olivine under deep Earth conditions: Implications for core formation in the early solar system. *Phys. Earth Planet. Inter.* **263**, 38–54 (2017).
30. D. J. Frost, F. Langenhorst, The effect of Al_2O_3 on Fe–Mg partitioning between magnesiowüstite and magnesium silicate perovskite. *Earth Planet. Sci. Lett.* **199**, 227–241 (2002).
31. M. E. Zimmerman, S. Zhang, D. L. Kohlstedt, S.-i. Karato, Melt distribution in mantle rocks deformed in shear. *Geophys. Res. Lett.* **26**, 1505–1508 (1999).
32. M. C. Shannon, *Percolation of Iron Melts Through Mantle Minerals at High Pressure: Implications for Core Formation* (Harvard University, 1998).
33. J. Dong, J. Li, F. Zhu, Wetting behavior of iron-carbon melt in silicates at mid-mantle pressures with implications for Earth's deep carbon cycle. *Front. Earth Sci.* **7**, 268 (2019).
34. N. Tsujino, Y. Nishihara, D. Yamazaki, Y. Seto, Y. Higo, E. Takahashi, Mantle dynamics inferred from the crystallographic preferred orientation of bridgmanite. *Nature* **539**, 81–84 (2016).
35. G. Kaptay, Modelling interfacial energies in metallic system. *Mater. Sci. Forum* **473–474**, 1–10 (2005).
36. T. Yoshino, M. J. Walter, T. Katsura, Core formation in planetesimals triggered by permeable flow. *Nature* **422**, 154–157 (2003).
37. R. W. L. De Wit, J. Trampert, Robust constraints on average radial lower mantle anisotropy and consequences for composition and texture. *Earth Planet. Sci. Lett.* **429**, 101–109 (2015).
38. G. Hirth, D. Kohlstedt, Rheology of the upper mantle and the mantle wedge: A view from the experimentalists, in *Inside the Subduction Factory* (American Geophysical Union, 2003), pp. 83–105.
39. A. J. Brearley, R. H. Jones, J. J. Papike, Chondritic meteorites. *Planet. Mater. Rev. Mineral.* **36**, C1 (1998).
40. D. W. Mittlefehldt, T. J. McCoy, C. A. Goodrich, A. Kracher, Chapter 4. Non-chondritic meteorites from asteroidal bodies, in *Planetary Materials*, J. J. Papike, Ed. (De Gruyter, 1998), pp. 523–718.
41. D. McKenzie, Some remarks on the movement of small melt fractions in the mantle. *Earth Planet. Sci. Lett.* **95**, 53–72 (1989).
42. U. H. Faul, Permeability of partially molten upper mantle rocks from experiments and percolation theory. *J. Geophys. Res. Solid Earth* **102**, 10299–10311 (1997).
43. H. Terasaki, T. Kato, S. Urakawa, K.-i. Funakoshi, A. Suzuki, T. Okada, M. Maeda, J. Sato, T. Kubo, S. Kasai, The effect of temperature, pressure, and sulfur content on viscosity of the Fe–FeS melt. *Earth Planet. Sci. Lett.* **190**, 93–101 (2001).
44. N. Bagdassarov, G. Solferino, G. Golabek, M. Schmidt, Centrifuge assisted percolation of Fe–S melts in partially molten peridotite: Time constraints for planetary core formation. *Earth Planet. Sci. Lett.* **288**, 84–95 (2009).
45. M. T. L. Berg, G. D. Bromiley, Y. Le Godec, J. Philippe, M. Mezouar, J.-P. Perrillat, N. J. Potts, Rapid core formation in terrestrial planets by percolative flow: In-situ imaging of metallic melt migration under high pressure/temperature conditions. *Front. Earth Sci.* **6**, 77 (2018).

46. K. A. Todd, H. C. Watson, T. Yu, Y. Wang, The effects of shear deformation on planetesimal core segregation: Results from in situ x-ray micro-tomography. *Am. Mineral.* **101**, 1996–2004 (2016).
47. J. J. Roberts, J. H. Kinney, J. Siebert, F. J. Ryerson, Fe-Ni-S melt permeability in olivine: Implications for planetary core formation. *Geophys. Res. Lett.* **34**, L14306 (2007).
48. G. N. Riley Jr, D. L. Kohlstedt, Kinetics of melt migration in upper mantle-type rocks. *Earth Planet. Sci. Lett.* **105**, 500–521 (1991).
49. H. Fei, U. Faul, T. Katsura, The grain growth kinetics of bridgmanite at the topmost lower mantle. *Earth Planet. Sci. Lett.* **561**, 116820 (2021).
50. D. Abbott, L. Burgess, J. Longhi, W. H. Smith, An empirical thermal history of the Earth's upper mantle. *J. Geophys. Res. Solid Earth* **99**, 13835–13850 (1994).
51. T. Kleine, C. Münker, K. Mezger, H. Palme, Rapid accretion and early core formation on asteroids and the terrestrial planets from Hf–W chronometry. *Nature* **418**, 952–955 (2002).
52. Y. Zhang, Geochemical kinetics, in *Geochemical Kinetics* (Princeton University Press, 2021).
53. C. Holzapfel, D. C. Rubie, D. J. Frost, F. Langenhorst, Fe-Mg interdiffusion in (Mg,Fe)SiO_3 perovskite and lower mantle reequilibration. *Science* **309**, 1707–1710 (2005).
54. N. Takafuji, K. Hirose, M. Mitome, Y. Bando, Solubilities of O and Si in liquid iron in equilibrium with (Mg,Fe)SiO3 perovskite and the light elements in the core. *Geophys. Res. Lett.* **32**, L063631 (2005).
55. O. Tschauner, A. Zerr, S. Specht, A. Rocholl, R. Boehler, H. Palme, Partitioning of nickel and cobalt between silicate perovskite and metal at pressures up to 80 GPa. *Nature* **398**, 604–607 (1999).
56. U. Mann, D. J. Frost, D. C. Rubie, H. Becker, A. Audétat, Partitioning of Ru, Rh, Pd, Re, Ir and Pt between liquid metal and silicate at high pressures and high temperatures – Implications for the origin of highly siderophile element concentrations in the Earth's mantle. *Geochim. Cosmochim. Acta.* **84**, 593–613 (2012).
57. H. Keppler, D. J. Frost, Introduction to minerals under extreme conditions, in *Mineral Behavior at Extreme Conditions*, R. Miletcih, Ed. (European Mineralogical Union, 2005), vol. 7.
58. G. Fiquet, A. L. Auzende, J. Siebert, A. Corgne, H. Bureau, H. Ozawa, G. Garbarino, Melting of peridotite to 140 gigapascals. *Science* **329**, 1516–1518 (2010).
59. H. Palme, H. S. C. O'Neill, Cosmochemical estimates of mantle composition. *Treatise on geochemistry* **2**, 568 (2003).
60. W. McDonough, 2.15–Compositional model for the Earth's core. *Treatise Geochem.* **2**, 547–568 (2003).
61. Y. Kono, C. Kenney-Benson, Y. Shibazaki, C. Park, G. Shen, Y. Wang, High-pressure viscosity of liquid Fe and FeS revisited by falling sphere viscometry using ultrafast x-ray imaging. *Phys. Earth Planet. In.* **241**, 57–64 (2015).
62. S. Anzellini, A. Dewaele, M. Mezouar, P. Loubeyre, G. Morard, Melting of iron at Earth's inner core boundary based on fast x-ray diffraction. *Science* **340**, 464–466 (2013).
63. C. Holzapfel, S. Chakraborty, D. Rubie, D. J. Frost, Effect of pressure on Fe–Mg, Ni and Mn diffusion in $(Fe_xMg_{1-x})_2SiO_4$ olivine. *Phys. Earth Planet. In.* **162**, 186–198 (2007).
64. F. Nimmo, C. Agnor, Isotopic outcomes of N-body accretion simulations: Constraints on equilibration processes during large impacts from HfAV observations. *Earth Planet. Sci. Lett.* **243**, 26–43 (2006).

Acknowledgments: We acknowledge N. Walte and M. Walter for discussions of the manuscript. **Funding:** This research was supported by NASA grants to Y.F. (80NSSC20K0337 and NNX17AE30G) and a Carnegie fellowship. **Author contributions:** Conceptualization: L.W. and Y.F. Methodology: L.W. Investigation: L.W. Supervision: Y.F. Writing—original draft: L.W. Writing—review and editing: L.W. and Y.F. **Competing interests:** The authors declare that they have no competing interests. **Data and materials availability:** All data needed to evaluate the conclusions in the paper are present in the paper and/or the Supplementary Materials.

Submitted 7 August 2022
Accepted 11 January 2023
Published 15 February 2023
10.1126/sciadv.ade3010